Identification of an advanced hardening model for single phase steels

Muhammad Noman, Bob Svendsen
Department of Mechanical engineering, University of Dortmund ,
Dortmund, Germany

Summary:

Sheet metal forming processes cover a wide range of applications in industry. In order to model sheet metal forming processes using numerical simulation an accurate description of the material behavior is required. To this end a material model has been implemented which is capable of capturing the movement and proportional expansion of the yield surface along with the change in the shape of the yield surface. The former is described as kinematic and isotropic hardening, respectively, and the latter is termed as distortional (cross) hardening. Once the model is implemented the second step consists in identifying the material parameters. In this contribution, a strategy for the identification of material parameters is presented. The strategy is based on identifying the isotropic hardening, combined hardening (isotropic-kinematic hardening), and complete hardening model (isotropic-kinematic-cross hardening) sequentially, in such a way that the parameter values identified in the previous step are used as starting values for the next step. Hence, the isotropic and kinematic hardening are first identified using the monotonic shear and Bauschinger shear test data, then the distortional (cross) hardening effect is determined using orthogonal tension-shear data using the isotropic-kinematic hardening parameter values as starting values. The material model was implemented in LS-DYNA using user defined material and LS-OPT based parameter identification for the steels LH-800 and DC06 is performed. The identified parameters are first validated and then used in F.E. simulations using ABAQUS and LS-DYNA. A complete account on application of identified material model is presented in the talk ”Numerical investigation of draw bending and deep drawing taking into account cross hardening” presented at this meeting.

Keywords:

parameter identification, induced flow anisotropy, distortional hardening,isotropic-kinematic hardening, strain path changes, sheet forming

1 Introduction

The experimental and theoretical characterization of sheet metal forming continues to provide a number of challenges for theorist and experimentalist alike. Among the foremost issues in this regard is a realistic model for the material behavior involved. Metal forming processes generally involve large strain resulting in significant microstructural development and significant induced anisotropic hardening. In many sheet metals subject to complex loading, dislocation microstructure consisting of dislocation-poor cells surrounded by dislocation-rich walls develop. Such microstructure formation is accompanied by local residual stress state development and various types of hardening. In case of reverse (*i.e.*, Bauschinger) loading, for example, deformation is accomodated by slip on the same slip systems but in opposite direction. Excess dislocations oriented in the original loading direction induce a residual stress state in the reverse direction which effectively lowers the yield stress in this direction, representing the Bauschinger effect. In case of orthogonal (*e.g.*, tension-shear) loading path changes, the slip systems activated during the previous deformation become latent, and new slip system are activated. Depending on a number of factors, the dislocations structures associated with the now latent systems may act initially as obstacle to slip on the newly active slip system, resulting in a transient increase in yield strength in the orthogonal direction. Continued orthogonal loading results in a breakdown in these structures and their reformation in association with the active slip systems. Such a transient or dynamic increase in yield strength after an orthogonal loading path change results in a change in the shape of the yield surface as is known as cross or distortional hardening [*e.g.*,[6, 7, 8]].

The current work begins in Section 2 with a formulation of the current model in the framework of the multiplicative decomposition of the deformation gradient and based on micromechanical considerations. As in the approach of [7] and [9], the current approach accounts for both hardening stagnation after load reversal and for cross hardening after orthogonal loading-path changes. The effects of such processes on the mechanical behavior is investigated experimentally in the current work with the help of tension-shear and cyclic shear tests described. The experimental setup and details together with the basic results for the steels LH800 and s DC06 are described in Section 3. In Section 4, the strategy developed for model identification on the basis of the data from Section 3 is presented along with the results of this identification. The determination of parameter values for models like the current one emboding complex three-dimensional history-dependent higher-order tensorial behavior in a physically-meaningful way is also quite non-trivial. Different approaches and software are employed in the literature. These include the work of [10], who used the software SiDolo to identifiy the Teodosiu model including a sensitivity analysis. An optimization method that is mainly based on the Levenberg-Marquardt algorithm is used by [11] as based on the one-element FE package Lagamine [11]. Finally, the model identification is validated with the help of additional test results from the experiments described in Section 3.

2 Material Model formulation

The current material model formulation is carried out in the framework of the standard inelastic multiplicative decomposition $\mathbf{F} = \mathbf{F}_{\mathrm{E}}\mathbf{F}_{\mathrm{P}}$ of the deformation gradient $\mathbf{F}$ [*e.g.*,[12]]. Such a decomposition arises naturally, *e.g.*, in the context of the modeling of $\mathbf{F}_{\mathrm{P}}$ as a change of local reference configuration [13]. In this context, one obtains in particular the result

$$\mathbf{R}_{\mathrm{E}}^{\mathrm{T}}\mathbf{L}_{\mathrm{E}}\mathbf{R}_{\mathrm{E}} = \mathbf{R}_{\mathrm{E}}^{\mathrm{T}}\mathbf{L}\mathbf{R}_{\mathrm{E}} - \mathbf{U}_{\mathrm{E}}\mathbf{L}_{\mathrm{P}}\mathbf{U}_{\mathrm{E}}^{-\mathbf{1}} = \mathbf{R}_{\mathrm{E}}^{\mathrm{T}}\dot{\mathbf{R}}_{\mathrm{E}} + \dot{\mathbf{U}}_{\mathrm{E}}\mathbf{U}_{\mathrm{E}}^{-\mathbf{1}} \tag{1}$$

via the right polar decomposition $\mathbf{F}_{\mathrm{E}} = \mathbf{R}_{\mathrm{E}}\mathbf{U}_{\mathrm{E}}$ of $\mathbf{F}_{\mathrm{E}}$ for the back-rotated form of $\mathbf{L}_{\mathrm{E}} := \dot{\mathbf{F}}_{\mathrm{E}}\mathbf{F}_{\mathrm{E}}^{-\mathbf{1}}$ in terms of $\mathbf{L} := \dot{\mathbf{F}}\mathbf{F}^{-\mathbf{1}}$ and $\mathbf{L}_{\mathrm{P}} := \dot{\mathbf{F}}_{\mathrm{P}}\mathbf{F}_{\mathrm{P}}^{-\mathbf{1}}$. For the current case of polycrystalline metals and small elastic strain, we have

$$\begin{aligned} \mathbf{U}_{\mathrm{E}} &= \mathbf{I} + \ln\mathbf{U}_{\mathrm{E}} + \mathbf{O}(\mathbf{2}) \,, \\ \dot{\mathbf{U}}_{\mathrm{E}}\mathbf{U}_{\mathrm{E}}^{-\mathbf{1}} &= \overline{\ln\mathbf{U}}_{\mathrm{E}}^{\cdot} + \mathbf{O}(\mathbf{2}) \,. \end{aligned} \tag{2}$$

Substituting these into (1), and taking the symmetric and skew-symmetric parts of the result, one obtains the evolution relations

$$\begin{aligned} \overline{\ln \mathbf{U}}_{\mathrm{E}} &= \mathbf{R}_{\mathrm{E}}^{\mathrm{T}} \mathbf{D} \mathbf{R}_{\mathrm{E}} - \mathbf{D}_{\mathrm{P}} \,, \\ \dot{\mathbf{R}}_{\mathrm{E}} &= \mathbf{W} \mathbf{R}_{\mathrm{E}} - \mathbf{R}_{\mathrm{E}} \mathbf{W}_{\mathrm{P}} \,, \end{aligned} \tag{3}$$

for $\ln \mathbf{U}_{\mathrm{E}}$ and $\mathbf{R}_{\mathrm{E}}$, respectively, in the incremental context. $\mathbf{D} := \mathrm{sym}(\mathbf{L})$ is the continuum rate of deformation, $\mathbf{D}_{\mathrm{P}} := \mathrm{sym}(\mathbf{L}_{\mathrm{P}})$ its inelastic counterpart, $\mathbf{W} := \mathrm{skw}(\mathbf{L})$ the continuum spin, and $\mathbf{W}_{\mathrm{P}} := \mathrm{skw}(\mathbf{L}_{\mathrm{P}})$ the plastic spin. Restricting the current formulation to the case of sheet metal forming, it is reasonable to assume that the texture in these materials achieved during rolling remains largely unchanged during forming processes like tension, compression, simple shear, cyclic simple shear, and combinations of these. In this case, $\mathbf{W}_{\mathrm{P}}$ is negligible, and the evolution of $\mathbf{R}_{\mathrm{E}}$ depends only on $\mathbf{W}$, in which case it reduces to a purely kinematic quantity (*i.e.*, the Jaumann rotation). In addition, focusing in this work on the material behavior of sheet metal during forming below the forming limit, we assume for simplicity that damage or any other process resulting in inelastic volume changes are neglible. In this case, plastic incompressibility $\det(\mathbf{F}_{\mathrm{P}}) = 1$ pertains, implying $\mathrm{tr}(\mathbf{D}_{\mathrm{P}}) = 0$ and $\mathbf{D}'_{\mathrm{P}} = \mathbf{D}_{\mathrm{P}}$ in the incremental context.

Since the elastic range and elastic strain are small, any texture effects from rolling leading to an anisotropic elastic behavior are assumed negligible. In this case, the isotropic form

$$\mathbf{M} = \kappa \, \mathrm{tr}(\mathbf{E}_{\mathrm{E}}) \, \mathbf{I} + 2 \mu \, \mathbf{E}'_{\mathrm{E}} \tag{4}$$

is assumed for the Mandel stress $\mathbf{M}$ in terms of the elastic strain $\mathbf{E}_{\mathrm{E}} := \ln \mathbf{U}_{\mathrm{E}}$, bulk modulus κ, shear modulus μ, and deviatoric part $\mathbf{E}'_{\mathrm{E}}$ of $\mathbf{E}_{\mathrm{E}}$. Lastly, again in the framework of small elastic strain, $\mathbf{M}$ and $\mathbf{R}_{\mathrm{E}}$ determine the Kirchhoff stress $\mathbf{K}$ via

$$\mathbf{K} = \mathbf{R}_{\mathrm{E}} \mathbf{M} \mathbf{R}_{\mathrm{E}}^{\mathrm{T}} \,. \tag{5}$$

Consequently, in contrast to $\mathbf{K}' = \mathbf{R}_{\mathrm{E}} \mathbf{M}' \mathbf{R}_{\mathrm{E}}^{\mathrm{T}}$, $\mathrm{tr}(\mathbf{K}) = \mathrm{tr}(\mathbf{M})$ of $\mathbf{K}$ is independent of $\mathbf{R}_{\mathrm{E}}$.

In this framework, then, the material behavior of polycrystalline sheet metal during forming processes below the forming limit is predominantly determined by a changing dislocation microstructure and attendant evolving anisotropic yield behavior. Besides a shift of the yield surface and its proportional expansion as in the case of conventional combined hardening, the current model also accounts for an evolving yield surface shape, *i.e.,* distortional or cross hardening. These are all reflected in the current yield surface model as given by the form

$$\phi = \sqrt{\Sigma \cdot \mathscr{A} \, \Sigma} - \sigma_{\mathrm{Y}} \,. \tag{6}$$

$\Sigma := \mathbf{M} - \mathbf{X}$ is the effective stress, $\mathbf{X}$ the back stress, and $\sigma_{\mathrm{Y}} := \sigma_{\mathrm{Y0}} + r$ is the yield stress, with σ_{Y0} its initial value. Further, $\mathscr{A}$ is an evolving fourth-order traceless symmetric tensor determining changes in shape of the yield surface due to microstructure development. For the class of materials under consideration, the evolution of r is modeled by the Voce form

$$\dot{r} = c_r \, (s_r - r) \, \dot{\alpha}_{\mathrm{P}} \tag{7}$$

in terms of the corresponding saturation rate c_r, and saturation value s_r, associated with r. α_{P} is the accumulated equivalent inelastic deformation. The initial value r_0 of r is given by the initial yield stress. In the current rate-independent context, α_{P} is determined as usual by the consistency condition. Analogous to the isotropic case, kinematic hardening is modeled via the Armstrong-Frederick form

$$\dot{\mathbf{X}} = c_x \, (s_x \mathbf{N}_{\mathrm{P}} - \mathbf{X}) \, \dot{\alpha}_{\mathrm{P}} \tag{8}$$

for kinematic hardening and the evolution of the back stress $\mathbf{X}$ depending on corresponding saturation rate c_x and saturation magnitude s_x associated with $\mathbf{X}$. $\mathbf{N}_{\mathrm{P}} := \mathbf{D}_{\mathrm{P}} / |\mathbf{D}_{\mathrm{P}}|$ is the direction of the rate of inelastic deformation

$$\mathbf{D}_{\mathrm{P}} = \dot{\alpha}_{\mathrm{P}} \, \partial_{\Sigma} \, \phi \tag{9}$$

modeled in associated form. The initial value of $\mathbf{X}$ is assumed to be zero. The current model is completed by the evolution relation

$$\dot{\mathscr{A}} = c_d \{s_d \mathscr{N}_{\mathrm{P}} - \mathscr{A}_d\} \dot{\alpha}_{\mathrm{P}} + c_l \{s_l (\mathscr{I}_{\mathrm{dev}} - \mathscr{N}_{\mathrm{P}}) - \mathscr{A}_l\} \dot{\alpha}_{\mathrm{P}} \tag{10}$$

for $\mathscr{A}$ with $\mathscr{N}_{\mathrm{P}} := \mathbf{N}_{\mathrm{P}} \otimes \mathbf{N}_{\mathrm{P}}$. $\mathscr{I}_{\mathrm{dev}}$ is the deviatoric part of the fourth-order identity tensor, $\mathscr{A}_d = (\mathscr{N}_{\mathrm{P}} \cdot \mathscr{A})\, \mathscr{N}_{\mathrm{P}}$ is the projection of $\mathscr{A}$ parallel, and $\mathscr{A}_l = \mathscr{A} - \mathscr{A}_d$ is the projection of $\mathscr{A}$ orthogonal, to $\mathbf{N}_{\mathrm{P}}$. Analogous to (8), this form is based on the idea of growth and saturation of the dynamic (*i.e.*, current) $\mathscr{A}_d$ and latent $\mathscr{A}_l$ parts of $\mathscr{A}$. In particular, c_d represents the saturation rate, and s_d the saturation magnitude, associated with $\mathscr{A}_d$. Analogously, c_l represents the saturation rate, and s_l the saturation magnitude, associated with $\mathscr{A}_l$. The initial value $\mathscr{A}_0$ of $\mathscr{A}$ is determined by any Hill initial flow othotropy due to any texture from rolling.

The current material model was implemented in the commercial FE codes Abaqus and LS-Dyna via the user material interfaces provided. Besides the two elasticity parameters κ, μ and the 6 parameters (*e.g.*, in the sense of Hill: F, G, H, L, M, N) for the initial flow orthotropy, this model contains 8 hardening parameters c_r, s_r, c_x, s_x, c_d, s_d, c_l, s_l to be identified using the tests to be described next.

3 Experimental results

The tests were performed by means of biaxial testing machine at Netherlands Institute for Metals Research, University of Twente. The tests performed on the steel LH800 and Steel DC06 consist of reverse simple shear test with different amounts of pre-strains; plane strain tension tests with different strain rates and orthogonal tests with and without unloading. Figure 1 shows the results of 2 reverse tests in simple shear for the two steels.The Bauschinger effect is clearly observed in this figure. For both tests,there is no clear elasto-plastic transition in the reverse stroke visible.

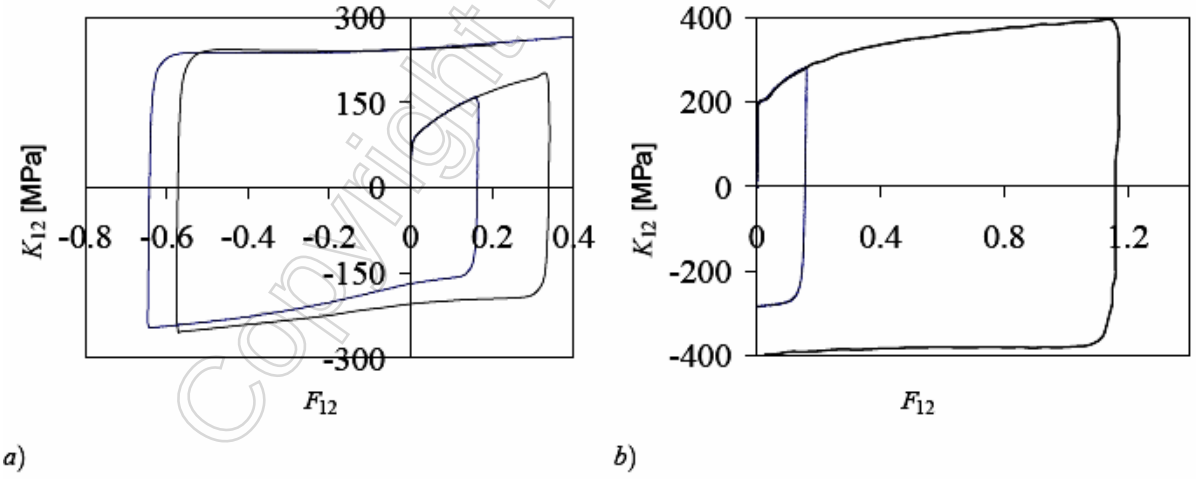

Figure 1: Reverse shear tests. $a)$ steel DC06. $b)$ steel LH800. Here K_{12} represents the shear component of Kirchoff stress and F_{12} represents component of deformation gradient.

Lastly, consider the results from the orthogonal tests. As stated above, these consist of plane-strain tension followed by simple shear. The transition from tension to simple shear is carried out either discontinuously via intermediate unloading, or continuously from tension to shear at yield, as shown in Figure 2. For the latter case, 5 different transition paths have been investigated (Figure 3). In the one extreme (path 1), the orthogonal change is realized via an ”abrupt” reduction in tension and coincident increase in shear at yield. This is closest to the case of a discontinuous orthogonal loading-path change (Figure 2). In the other extreme (curve 5), the level of tension is maintained (and further tensile

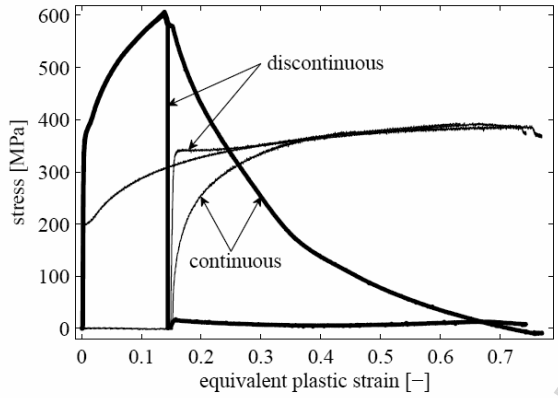

Figure 2: Orthogonal experiments on steel LH800 with and without elastic unloading

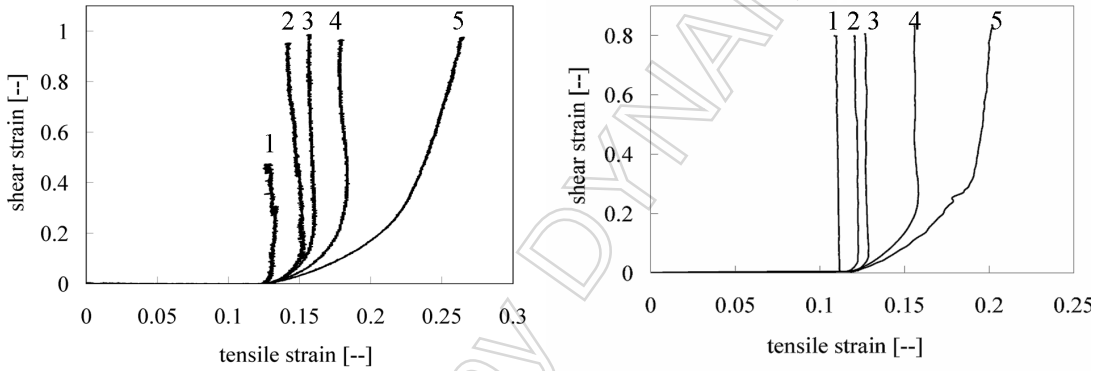

Figure 3: Experimental strain paths in the investigated steels resulting from continuous change of loading direction from tension to shear. Leftt: steel LH800. Right: steel DC06

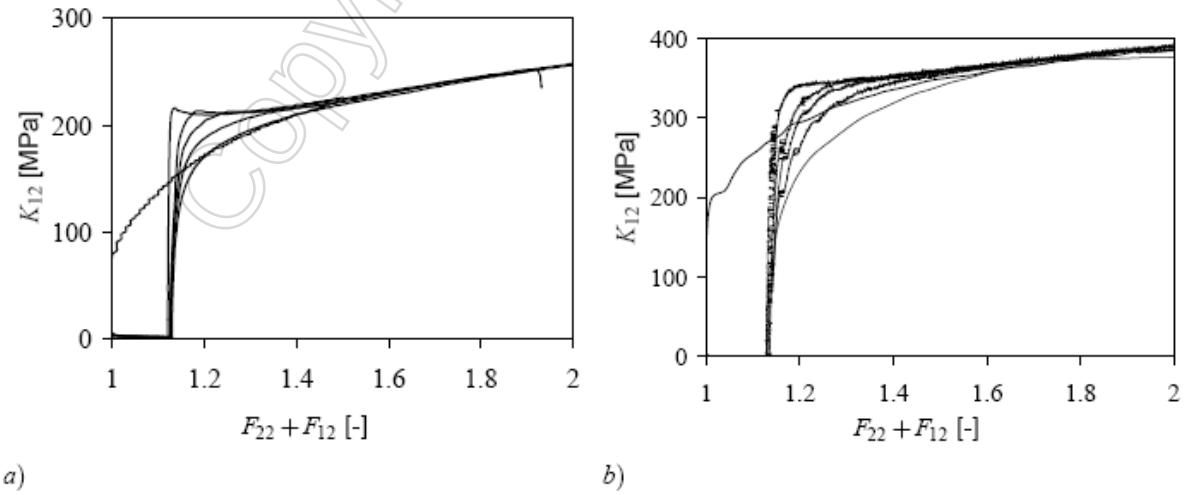

Figure 4: Orthogonal tests with different rate of transition from plane strain tension to simple shear. $a)$ steel DC06. $b)$ steel LH800. Here K_{12} represents the shear component of Kirchoff stress, F_{22} and F_{12} represent components of deformation gradient.

deformation occurs) as shear loading increases. As indicated, the other three curves (2, 3, and 4) in Figure 3 represent intermediate cases between these extremes. The corresponding stress-deformation results together with the forward simple-shear-based stress-deformation behavior of LH800 are depicted in Figure 4.

As implied by these results, the nature of the transition from tension to shear is crucial in determing whether or not cross hardening occurs. In cases 4 and 5, where further tension loading into the shear loading phase is most pronounced, for example, little or no cross hardening occurs. Asssuming that the dislocation microstructure developed during the common pre-tension phase was the same in each case, these results imply that continued tension loading during simultaneous shear loading at yield facilitates a breakdown of tension-based dislocation microstructure which would otherwise result in cross hardening upon transition to shear. Besides this, note that the paths with continued tension loading do not return to the monotonic simple-shear reference curve, i.e., at least not within the range of the experimental data. These and other aspects will be examined in more detail after we carry out the model identification, to which we now turn.

4 Model identification and validation

To demonstrate the capability of the presented model to describe the complex hardening behavior of the steels during non-proportional loading just discussed, we now turn to their identification. As shown by the results of the last section, this behavior involves in particular isotropic, kinematic, and cross, hardening. The material parameter determination is carried out using the program LS-OPT in conjunction with LS-DYNA. Given the homogeneous nature of the tests, one-element calculations suffice. The optimization technique used relies on response surface methodology (RSM) [1], a mathematical method for constructing smooth approximations of functions in a design space. The approximations are based on results calculated at numerous points in the multi-dimensional design space. In our example, the material parameters are the design variables, and the model together with the data determine the objective function of the corresponding optimization problem.

The fit strategy, and in particular the determination of reasonable starting values for the iterative determination of material parameter values, exploits the physics of the problem, tests and model. To this end, forward simple-shear loading data are used to identify the isotropic hardening model assuming no kinematic or cross hardening. The corresponding parameter values are then used as starting values to identify the isotropic-kinematic hardening model using data for both forward- and forward-reverse-shear loading. Analogously, the parameter values from this fit are used as starting values for a fit of the isotropic-kinematic-cross (*i.e.*, complete) hardening model to forward-shear, forward-reverse-shear, and tension-shear, loading data. All these fits are based on the fixed values $\kappa = 167.05$ GPa and $\mu = 77.09$ for the steel LH800 and $\kappa = 158.33$ and $\mu = 73.07$ GPa for the steel DC06, for the elastic properties, as well as that $\sigma_{Y0} = 330.79$ and $\sigma_{Y0} = 134.353$ MPa for the initial yield stresses at room temperature for the steel LH800 and the steel DC06 respectively.

We begin with the identification of the Voce isotropic hardening model using forward simple-shear data. The values for the Voce hardening model parameters so obtained are given in Table1. The quality of the fit can be judged via the comparison of the fitted model with the data in Figure 5.

Parameter	Value	Units
s_r	252.489	MPa
c_r	8.289	

$a)$

Parameter	Value	Units
s_r	341.504	MPa
c_r	5.8206	

$b)$

Table 1: isotropic hardening parameter values determined from forward simple-shear test data alone: $a)$ steel DC06 $b)$ steel LH800

Consider next the isotropic-kinematic case. An initial estimate for s_x is obtained via the shift in yield stress between forward and reverse shear. Using this together with isotropic hardening parameter values from the forward-shear case, the isotropic-kinematic hardening parameters were determined with the help of corresponding tests. The set of identified parameter values is given in Table 2. As before, the quality of

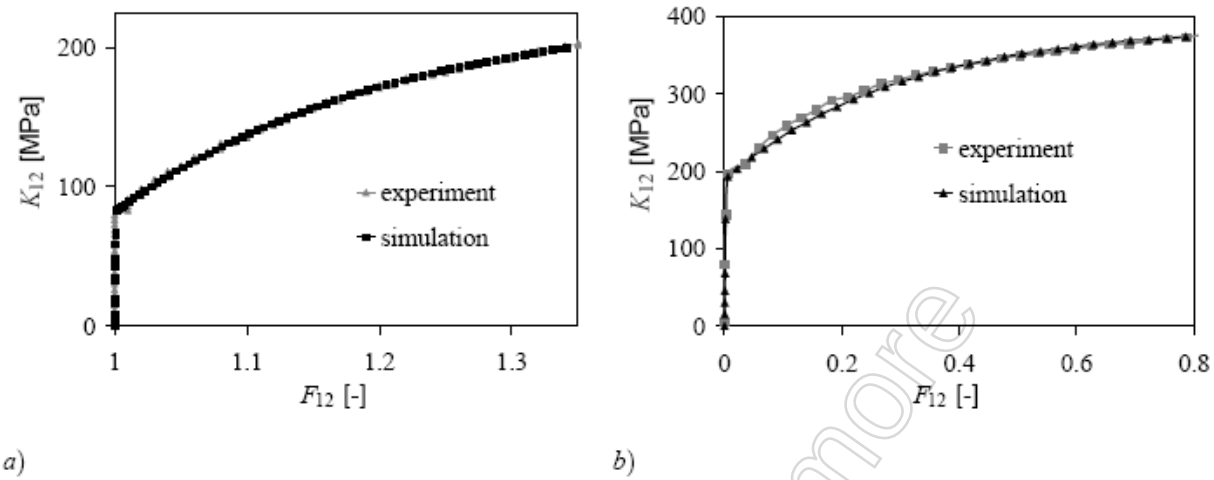

a) *b)*

Figure 5: Comparison of experimental and numerical results for Voce isotropic model. $a)$ steel DC06 . $b)$ steel LH800. Here K_{12} represents the shear component of Kirchoff stress and F_{12} represents component of deformation gradient.

Parameter	Value	Units
s_r	240.925	MPa
c_r	4.707	
s_x	62.5478	MPa
c_x	45.4374	

a)

Parameter	Value	Units
s_r	219.727	MPa
c_r	2.96	
s_x	139.625	MPa
c_x	15.1893	

b)

Table 2: isotropic-kinematic hardening parameters determined from forward- und forward-reverse simple-shear test data alone: $a)$ steel DC06 $b)$ steel LH800

the model identification can be judged via comparison with the fit data as shown for the current isotropic-kinematic hardening case in Figure 6.

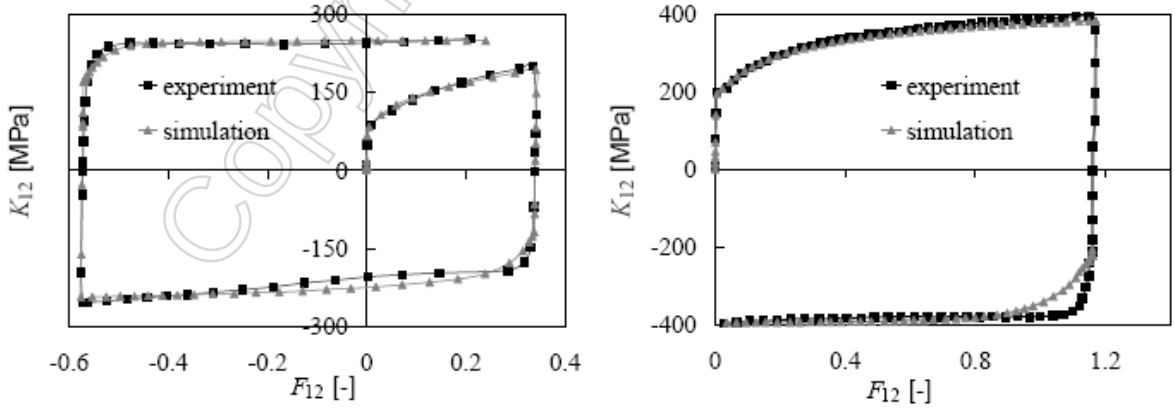

a) *b)*

Figure 6: Comparison of experimental forward-reverse shear data with the identified isotropic-kinematic hardening model. $a)$ steel DC06. $b)$ steel LH800. Here K_{12} represents the shear component of Kirchoff stress and F_{12} represents component of deformation gradient.

Before we proceed to the complete hardening model, it is instructive to compare the prediction of the

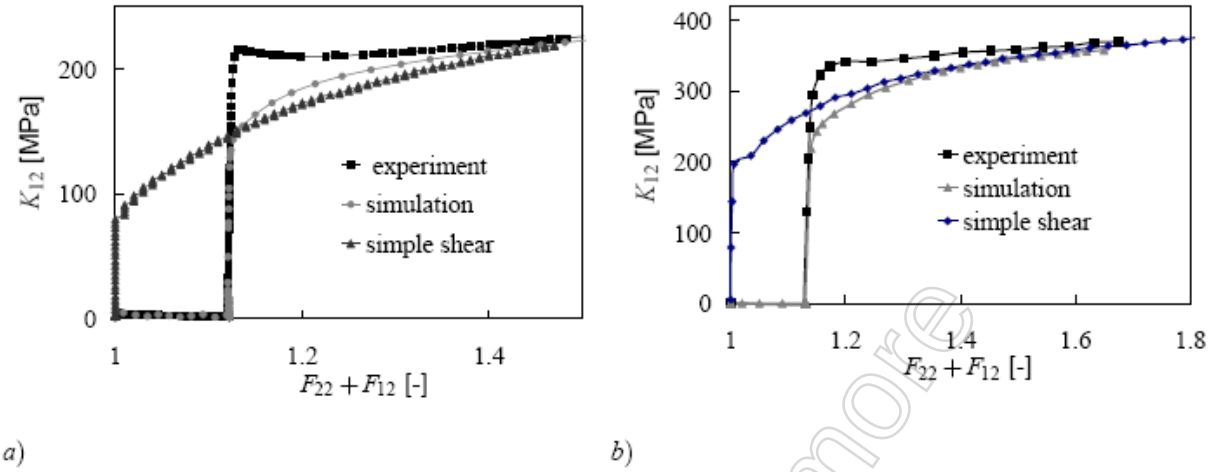

Figure 7: Comparison of identified Combined hardening model for the forward simple shear and orthogonal tension-shear test data. $a)$ steel DC06 . $b)$ steel LH800. Here K_{12} represents the shear component of Kirchoff stress, F_{22} and F_{12} represent components of deformation gradient.

combined hardening model just identified for the case of orthogonal tension-shear loading with the corresponding test data represented by path 1 in Figure 3. This in done in Figure 7. Not suprisingly, the model predicts no cross hardening. Optically, one might be tempted to identify the prediction of the identified combined model with case 4 or 5 in Figure 3. Since these represent different paths in either strain or stress space, however, they are not directly comparible.

Consider lastly the identification of the isotropic-kinematic-cross (*i.e.*, complete) hardening model. Again, this is done with the help of the identified parameter values for the isotropic-kinematic case as starting values for the fit. In addition, s_d contrained to be 0 and s_l is constrained to be less that 0. For the identification, the test data of path 1 in Figure 3 is added to the previous data sets. The results of this identification are presented in Table 3. The comparison of the corresponding experimental data and model fit is shown in Figure 8.

Parameter	Value	Units
s_r	240.925	MPa
c_r	4.707	
s_x	62.5478	MPa
c_x	45.4374	
s_d	0.0	
c_d	16.8335	
s_l	-0.922	
c_l	7	

$a)$

Parameter	Value	Units
s_r	219.727	MPa
c_r	2.96	
s_x	139.625	MPa
c_x	15.1893	
s_d	0.0	
c_d	8.29	
s_l	-0.86	
c_l	5.0	

$b)$

Table 3: isotropic-kinematic-cross hardening model parameter values determined from forward shear, forward-reverse shear, and from tension-shear, test data: $a)$ steel DC06 $b)$ steel LH800

As a first validation of the model identification presented in this section, we use the identified isotropic-kinematic-cross hardening model to simulate the behavior of steels along the (other) experimental strain paths 2 to 5 in Figure 3. The results are shown in Figure 9 and Figure 10 for the steels DC06 and LH800 respectively. Clearly, the agreement between experimental and simulation results is good. Hence, beyond the realistic representation of complete isotropic-kinematic-cross hardening behavior, the current model is also capable of accounting for the dependence of the amount of cross hardening arising on the nature and details of the orthogonal transition from tension to shear.

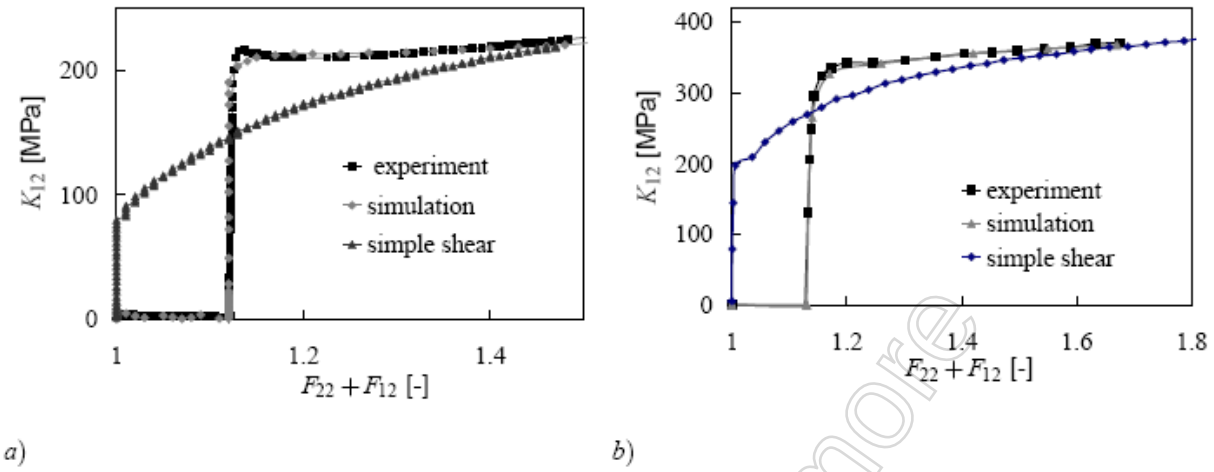

Figure 8: Comparison of the identified isotropic-kinematic-cross hardening model behavior with experimental data for monotonic forward simple shear and orthogonal tension-shear test data. $a)$ steel DC06 . $b)$ steel LH800. Here K_{12} represents the shear component of Kirchoff stress, F_{22} and F_{12} represent component of deformations gradient.

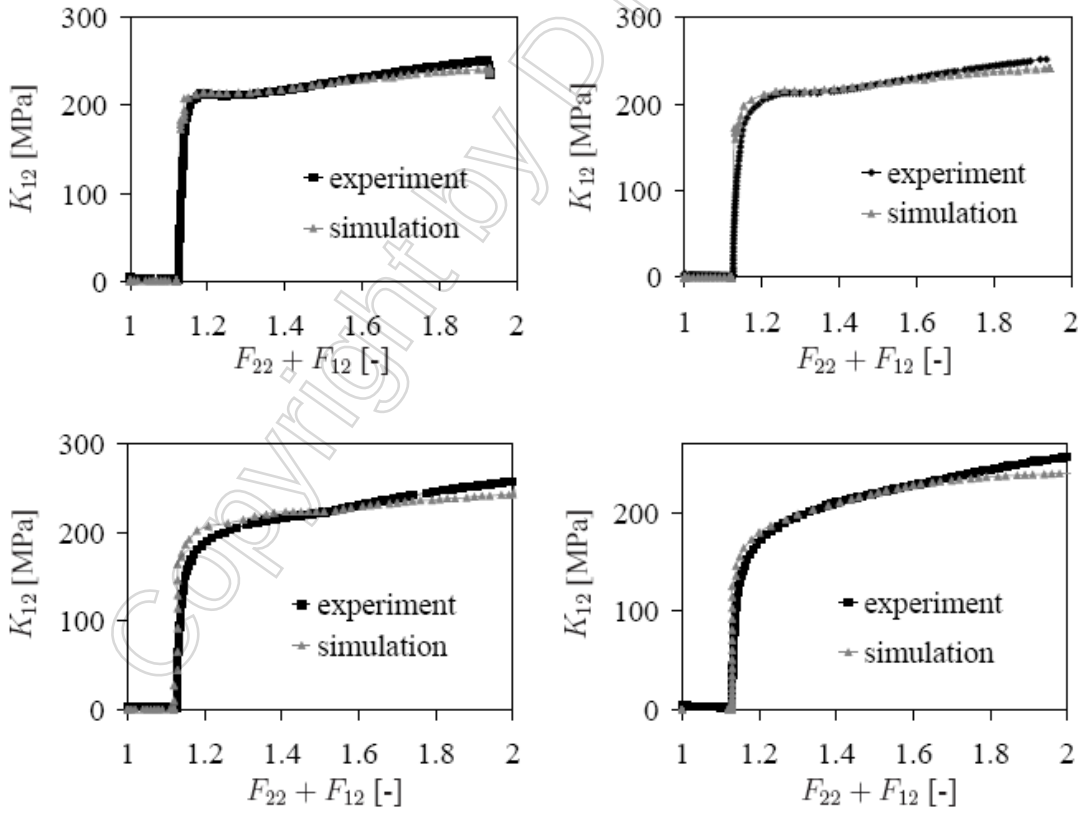

Figure 9: Comparison of the experimental results for strain paths 2 to 5 in Figure 3 (right) with corresponding simulation results as based on the identified model for isotropic-kinematic-cross hardening. Upper left: path 5. Upper right: path 4. Lower left: path 3. Lower right: path 2. Here K_{12} represents the shear component of Kirchoff stress and F_{22} and F_{12} represents components of deformation gradient.

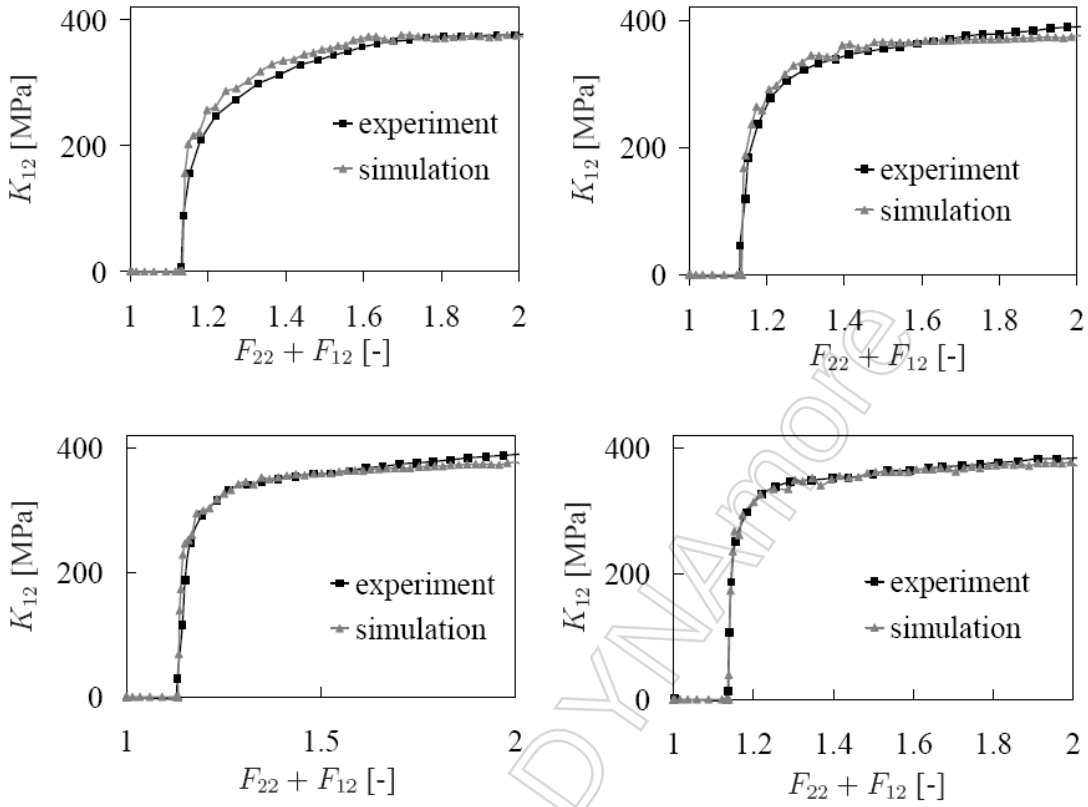

Figure 10: Comparison of the experimental results for strain paths 2 to 5 in Figure 3 (left) with corresponding simulation results as based on the identified model for isotropic-kinematic-cross hardening. Upper left: path 5. Upper right: path 4. Lower left: path 3. Lower right: path 2. Here K_{12} represents the shear component of Kirchoff stress and F_{22} and F_{12} represents components of deformation gradient.

5 Literature

[1] N. Stander, W. Roux, T. Eggleston and K. Craig: LS-OPT Users Manual: A design optimization and probabilistic analysis tool for the engineering analyst. Livermore Software Technology Corporation, Livermore, California, 2006

[2] B. Peeters, S.R. Kalidindi, C. Teodosiu, P. Van Houtte and E. Aernoudt: A theoretical investigation of the influence of dislocation sheets on evolution of yield surfaces in single-phase b.c.c. Polycrystals. Journal of the Mechanics and Physics of Solids , Volume 50 ,783-807,2002

[3] Levkovitch, V., Svendsen, B., Wang,: Micromechanically motivated phenomenological modeling of induced flow anisotropy and its application to metal forming processes with complex strain path changes. The 9th International ESAFORM Conference on Material Forming,Glasgow, UK, April 26-28, 2006.

[4] W.A. Sptitzig, R.J. Sober and O. Richmond: The effect of hydrostatic pressure on the deformation behavior of maraging and HY-80 steels and its implication for plasticity theory. Journal,Metal. Trans. A 7A:pp. 1703-1710, 1976

[5] S. Bouvier, J.L. Alves, M.C. Oliveira and L.F. Menezes: Modelling of anisotropic work-hardening behaviour of metallic materials subjected to strain path changes. Comp. Mater. Sci, 32 (2005):pp. 301-315, 2005

[6] C. Teodosiu, and Z. Hu : Evolution of the intragranular microstructure at moderate and large strains:

modelling and computational significanc. Shen, S.F., Dawson, P.R., Simulation of Materials Processing: Theory, Methods and Applications, Balkema, Rotterdam pages=173-182, 1995

[7] C. Teodosiu, and Z. Hu : Microstructure in the continuum modelling of plastic anisotropy., booktitle = Proceedings of 19th Risø International Symposium on Material's Science: Modelling of Structure and Mechanics of Materials from Microscale to Product, Risø National Laboratory, Roskilde, Denmark pages = 149-168, 1998

[8] S. Bouvier, J.L. Alves, M.C. Oliveira, and L.F. Menezes, : Modelling of anisotropic work-hardening behaviour of metallic materials subjected to strain-path changes. Computational Materials Science, Volume(32):301-315, 2005

[9] J. Wang, V. Levokovitch, F. Reusch, B.Svendsen, J. Huétink, and M. van. Riel, : On the modeling of hardening in metals during non-proportional loading. International Journal of Plasticity, Volume(24):10391070, 2008

[10] H. Haddadi, S. Bouvier, M. Banu, C. Maier, and C. Teodosiu, : Towards an accurate description of the anisotropic behaviour of sheet metals under large plastic deformations: modelling, numerical analysis and identification. International Journal of Plasticity, Volume(22):2226-2271, 2006

[11] P. Flores, L. Duchene,and C. Bouffioux , T. Lelotte , C. Henrard , and N. Pernin , A. Van Bael , S. He, J. Duflou and A.M. Habraken,: Model identification and FE simulations: Effect of different yield loci and hardening laws in sheet forming. International Journal of Plasticity, Volume(23):420449, 2007

[12] J. C. Simo, and T. J. R. Hughes, : Computational Inelasticity. Springer Verlag, 1998

[13] B. Svendsen, : On the modeling of anisotropic elastic and inelastic material behaviour at large deformation. International Journal of Solids and Structures, Volume(38):9579-9599, 2001